Journal of Nuclear Materials 538 (2020) 152230

Contents lists available at ScienceDirect

Journal of Nuclear Materials

journal homepage: www.elsevier.com/locate/jnucmat

Characterisation of open volume defects in Fe–Cr and ODS Fe–Cr alloys after He^+ and Fe^+ ion irradiations

M. Šćepanović [a, *], V. de Castro [a], I. García-Cortés [b], F.J. Sánchez [b], T. Gigl [c], C. Hugenschmidt [c], T. Leguey [a]

[a] Departamento de Física. Universidad Carlos III de Madrid, 28911, Leganés, Spain
[b] Laboratorio Nacional de Fusión, CIEMAT, Avda. de la Complutense 40, 28040, Madrid, Spain
[c] FRM II and Physics Department, Technische Universität München, 85747, Garching, Germany

ARTICLE INFO

Article history:
Received 12 February 2020
Received in revised form
24 April 2020
Accepted 6 May 2020
Available online 19 May 2020

Keywords:
Slow positron beam
Positron annihilation spectroscopy
FeCr alloys
ODS steels
Ion irradiation
Transmission electron microscopy

ABSTRACT

Different ODS RAF steels with nominal composition Fe–14Cr–2W–0.3-Ti–0.3Y_2O_3 (wt%) and a model Fe–14Cr (wt%) alloy have been subjected to single Fe^+ or He^+ ion irradiations to simulate the effect of a fusion environment at different doses and temperatures. The irradiation induced open volume defects have been characterised by positron annihilation spectroscopy and transmission electron microscopy. For low temperature Fe^+ irradiations, positron annihilation spectroscopy results show a high concentration of irradiation induced vacancy clusters, much more evident in the model alloy as compared to the ODS steels. The extent of damage due to He^+ irradiations at RT and high temperatures is considerably lower than for the Fe^+ irradiations. Regardless of the temperature He^+ irradiations introduced changes in the chemical environment of open-volume positron traps possibly due to the creation of He-vacancy complexes. Positron annihilation spectroscopy results also suggest that irradiation induced vacancy-type defects in ODS steels are not associated with nanoparticles but are mainly in the ferritic matrix. The presence of irradiation induced bubbles was studied after He^+ irradiation at high temperatures. Small bubbles were observed, being smaller in the ODS steels as compared to the model alloy.

1. Introduction

Nuclear fusion energy is nowadays considered one of the most promising alternatives for the fossil fuels that could satisfy both the increasing demand for energy across the globe and the reduction of CO_2 emissions and their effects on climate change [1,2]. At present, the experimental fusion reactor ITER, a tokamak magnetic confinement device, is being built in the southern part of France within a collaboration of 35 nations, as a crucial project for advancement of fusion reactors knowledge [3].

In-vessel structural materials of a nuclear fusion reactor will be subjected to high mechanical, electromagnetic and heat loads, and high neutron fluxes. Chosen materials will have to sustain the damage produced by the 14 MeV neutron irradiation, temperatures up to 700 °C, and large amounts of He produced in the material by transmutation reactions [4,5]. The materials need to have good mechanical behaviour at high temperatures, withstand high heat flux and thermal shocks, and have a good thermal conductivity and resistance to radiation damage. They should also satisfy the requirement of low activation so that if activated during the operation lifetime the half-life will be so small that after 50–100 years the radioactivity will be negligible [6]. Under neutron irradiation, the diffusion, agglomeration and interaction of existing and newly introduced interstitials and vacancies can profoundly change the properties of the material. Hence when designing radiation resistance materials for nuclear reactors there are some design options to be considered: use of matrix phases that show radiation tolerance, materials in which diffusion of vacancies is low at operational temperatures or materials with high densities of point defect sinks [7].

The performance of reduced activation ferritic-martensitic and ferritic steels for nuclear applications can be improved by oxide dispersion strengthening with small particles of Y_2O_3 and/or other rare earth oxides dispersed throughout the matrix [8–12]. Oxide dispersion strengthened (ODS) steels are characterised by a high

* Corresponding author. Department of Physics, Universidad Carlos III de Madrid, Avda. de la Universidad 30, 28911, Leganes, Madrid, Spain.
E-mail address: mscepano@fis.uc3m.es (M. Šćepanović).

https://doi.org/10.1016/j.jnucmat.2020.152230
0022-3115/

Table 1
Fabrication parameters.

Name	Nominal Composition (wt%)	Mechanical alloying	Processing	Heat treatment	Mean size of Y–Ti–O (nm)	Number density of Y–Ti–O ($\times 10^{22}$ m^{-3})
Fe14Cr	Fe–14Cr	–	Vacuum melted, Hot rolled	850 °C, 2 h	–	–
ODS1	Fe–14Cr–2W-0.3Ti-0.3Y_2O_3	Planetary ball mill Precursor Y_2O_3	HIP 2 h, 1100 °C, 200 MPa Forged 1150 °C	850 °C, 2 h	8 ± 5	2.4 ± 0.5
ODS2			HIP 2 h, 1100 °C, 175 MPa Hot Cross Rolled 1200 °C	1000 °C, 2 h	4 ± 2	6.3 ± 1.1
ODS3		Attritor mill Precursor Fe_2Y	HIP 2 h, 1100 °C, 175 MPa Hot Cross Rolled 900 °C	800 °C, 2 h	8 ± 6	14 ± 3

density of dislocations and fine grains. They exhibit superior high temperature tensile and creep properties when compared to reduced activation ferritic-martensitic (RAFM) steels [13]. Dispersed nano-oxides could act as traps for irradiation-induced He bubbles, thus inhibiting void swelling at high temperatures and accumulations at grain boundaries causing embrittlement. Small He bubbles can also act as centres for recombination of self-interstitials and vacancies [12]. This mechanism, however, might be different as helium-vacancy clusters may absorb vacancies, or absorb helium, depending on the He/vacancy ratio [14].

Neutron irradiation damage, coming from the damage induced by the primary knock-on atom, can be simulated by using heavy ion irradiation. Ion irradiation experiments are performed in a very controlled manner with well-defined temperature, energy and dose while avoiding high residual radioactivity [15], although the damage is confined to the near-surface regions, being non-uniform and with deposition of foreign ions. Self-ion irradiation is often employed in order to obtain a high amount of displacement damage without introducing impurities into the sample. The effects of He and H transmutation gasses on the irradiated material can also be investigated employing He and H irradiations which help to inform and calibrate models and to understand key processes behind radiation damage [16].

During the last decades there has been an considerable effort to characterise the effects of irradiation on RAFM, reduced activation ferritic (RAF), and ODS steels, (see for instance Refs. [9,17–19] and references therein), and to correlate those results with theoretical models describing the mechanisms governing the defect evolution and helium migration/retention [20–23]. However, the prediction of the radiation microstructure has yet to be accomplished and more investigations are necessary to clarify the effect of irradiation on these materials as a function of dose, dose-rate and temperature. The main objective of this work is to investigate the irradiation induced damage, focusing in open volume defects and irradiation induced bubbles, of ODS RAF steels and a model Fe14Cr alloy subjected to ion irradiations. For this purpose, single (Fe^+ or He^+), ion irradiations have been carried out at different doses and temperatures. The vacancy-type defects and bubbles induced by the irradiations have been characterised by slow Positron Annihilation Spectroscopy (PAS) and Transmission electron microscopy (TEM).

2. Experimental

Four different alloys have been investigated in this work; a model alloy (referred to as Fe14Cr) with nominal composition Fe-14 wt%Cr produced by Goodfellow. The material was vacuum melted, cast and rolled with annealing taking place during the processing. Its microstructure consists of dislocation-free large (~100 μm) equiaxed grains. Three different ODS steels with the same nominal composition Fe–14Cr–2W-0.3Ti-0.3Y_2O_3 (wt%), named as ODS1, ODS2 and ODS3, were produced by mechanical alloying, consolidated by hot isostatic pressing (HIP), processed either by forging or hot (cross) rolling and subsequently heat treated. Their detailed fabrication process can be found in Ref. [24–26]. Table 1 shows the most relevant fabrication parameters for each alloy. ODS1 shows a bimodal grain structure with recovered grains (sizes < 15 μm) and unrecovered submicron grains, while ODS2 and ODS3 show elongated partially recovered grains, most of them with submicron sizes, being the grain structure more homogeneous in ODS2. Apart from Cr–W-rich carbides and Ti-rich oxides, Y–Ti–O nanoparticles were observed homogeneously distributed in all the investigated ODS alloys. Their mean sizes and densities are also shown in Table 1.

Single Fe^+ ion irradiations were carried out in the Standard multipurpose line using 1 MeV Fe^+ ions at RT up to a fluence of 6.5 × 10^{15} ions/cm^2 at the CMAM facility [27,28]. Fig. 1a shows the implanted ions and damage profiles obtained from SRIM calculations. It must be noted that SRIM calculations are performed at 0 K

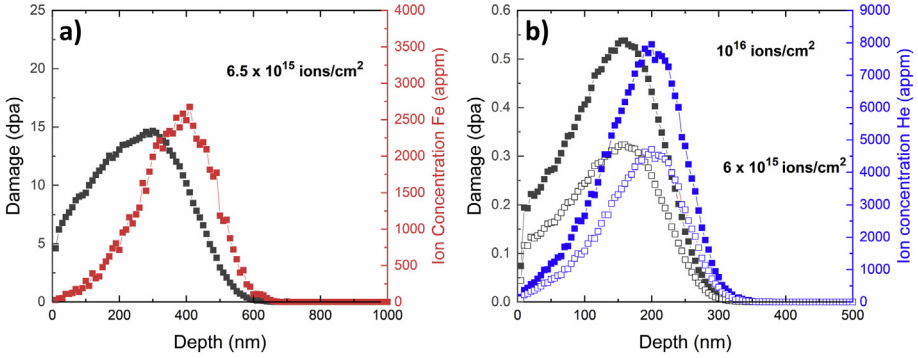

Fig. 1. Implantation profile and damage distribution as a function of depth calculated by SRIM for a) 1 MeV Fe^+ ions and b) 50 keV He^+ ions up to a maximum damage of 0.3 dpa (open symbols) and 0.5 dpa (full symbols).

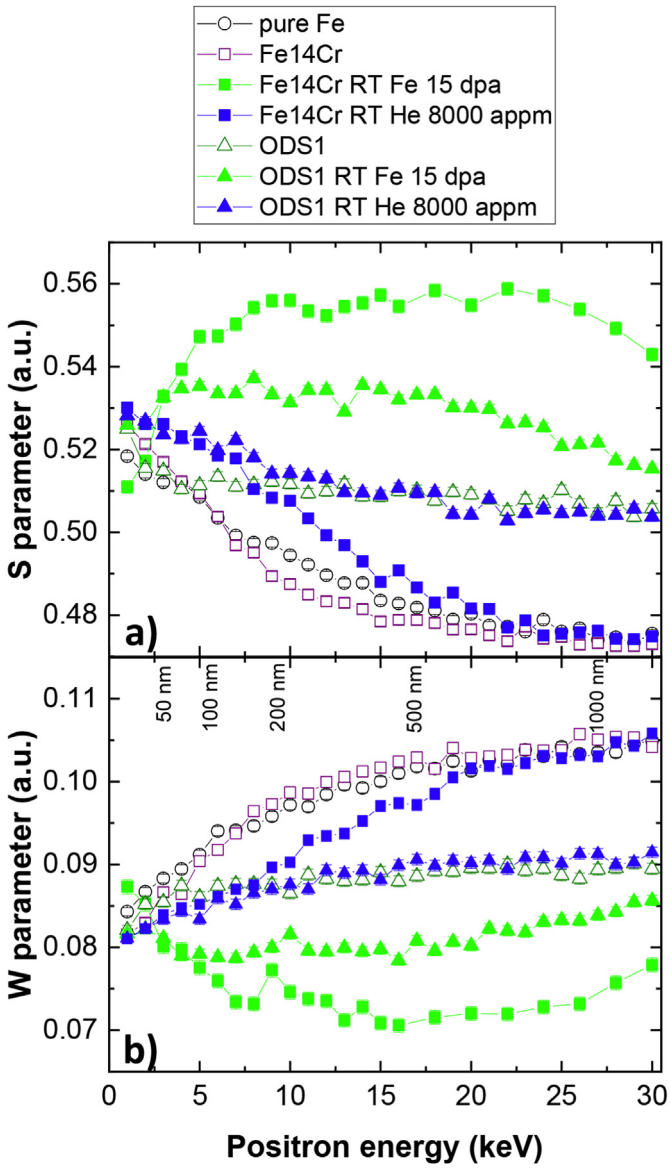

Fig. 2. a) S-parameter and b) W-parameter for pure Fe, the model Fe14Cr alloy and the ODS1 steel before and after the RT Fe^+ and RT He^+ irradiations as function of the incident positron energy.

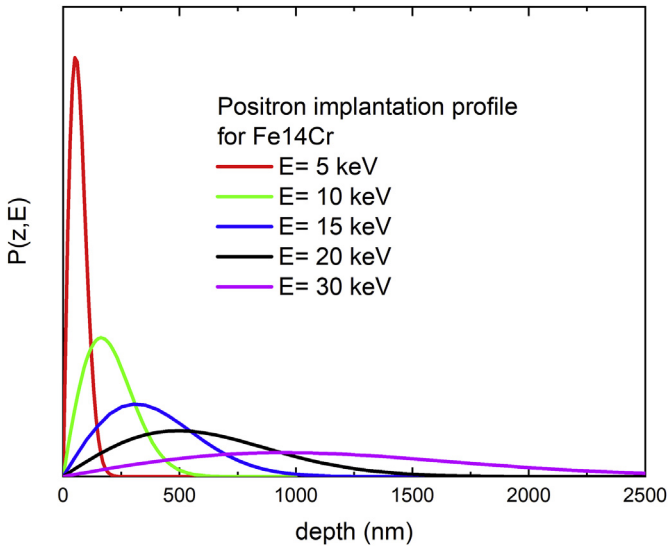

Fig. 3. Positron implantation profiles calculated for an Fe14Cr alloy at different positron energies.

so temperature effects are not taken into account, which can affect the actual depths of the damaged regions. The maximum damage peak obtained for this ion energy (Bragg peak) is located at around 300 nm from the sample surface. The maximum damage at the Bragg peak estimated using the Full Damage Cascades mode is 15 dpa. Displacement energies of 40 eV were used for Fe and Cr, following the ASTM standard E 521-96.

He^+ ion irradiations were performed at room temperature and 400 or 450 °C at the ion implanter in CIEMAT. Samples were irradiated with 50 keV He^+ ions up to fluences of 6.5×10^{15} ions/cm^2 and 10^{16} ions/cm^2. Fig. 1b shows the implantation profiles and damage distributions for these irradiations, as calculated by SRIM. The maximum He concentration reaches 4700 appm and 8000 appm at around 200 nm. The maximum damages, (0.3 dpa or 0.5 dpa respectively), are located at 160 nm (Bragg peak). As expected, the damage produced by He^+ ions is much lower than the one induced by the heavier Fe^+ ions.

Slow positron annihilation Doppler Broadening (DB) and Coincident Doppler Broadening (CDB) experiments were performed at NEPOMUC using positrons with energies up to 30 keV [29]. DB experiments were performed as a function of the incident positron energy, allowing to obtain depth profiles, while CDB experiments (more precise but also more time consuming) were realised only at selected positron energies. DB of the annihilation line gives information of the electron momentum by detecting gamma photons from the annihilation peak centred at 511 keV. The obtained spectrum is usually characterised by S and W parameters. The S-parameter is calculated as the ratio between the area of the central portion of the peak and its total area and hence quantifies the portion of positrons that have annihilated with lower momentum electrons. If the material contains open volume defects, they will trap positrons that will subsequently annihilate more likely with the low-momentum valence electrons, thus having a smaller deviation from 511 keV. This will result in a narrower distribution of the DB photo peak and hence an increase of the S-parameter. The W-parameter is the ratio of the high-energy portion of the peak and the total peak. It corresponds to the portion of positrons that have annihilated with the core electrons, which have higher momenta. The central window used for the S-parameter calculation was 1.632 keV, while the W-parameter was obtained from the higher momentum region in a range chosen from 514.26 to 515.9 keV. In order to remove the extensive background noise produced mostly by Compton scattering, and thus have a better resolution of the annihilation with high momentum core electrons, CDB uses two high purity Ge detectors detecting both annihilation gamma photons in coincidence. CDB spectra are usually normalised and presented as the ratio to a reference material with respect to the longitudinal component of the electron momentum. They can provide chemical information on the atoms surrounding the annihilation site [30]. The count rate of these measurements was about 300 s^{-1}. The total accumulated counts per spectrum were about 10^7.

Electron transparent samples for TEM observations were prepared by Focused Ion Beam (FIB). Thin lamellae were obtained by the lift-out technique with Pt deposition. The system was a Zeiss Auriga Compact scanning electron microscope equipped with a 30 kV Ga ion gun. Lower ion acceleration voltages (15–5 kV) were used in the final polishing stage to minimise surface damage.

TEM characterization was carried out using a JEOL JEM 3000F

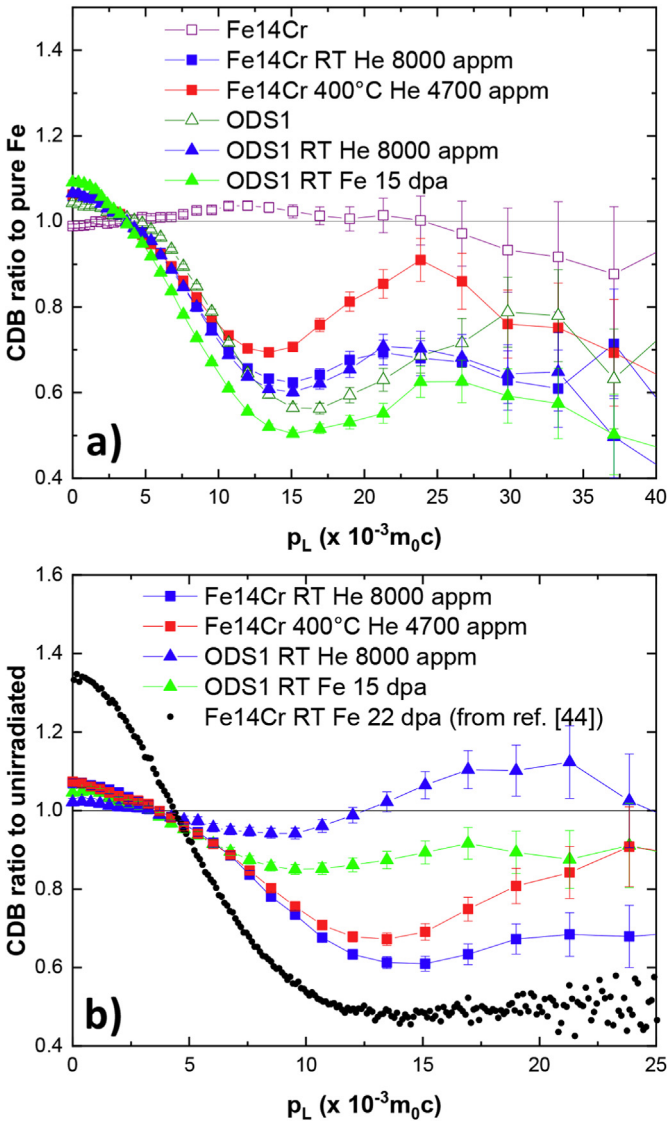

Fig. 4. a) CDB ratios to pure Fe of unirradiated and irradiated Fe14Cr and ODS1 steel. b) CDB ratios of irradiated Fe14Cr and ODS1 steel to their respective unirradiated samples.

microscope equipped with an X-ray energy dispersive spectrometer (XEDS) and an electron energy loss spectrometer (EELS) operated at 300 kV. Bubble number densities and sizes were measured from through-focal series in volumes in the order of 10^{-22} m^3. Bright field (BF) TEM images were under-focused or over-focused by 500 nm. The thicknesses of the regions analysed by TEM were obtained from EELS spectra.

3. Results and discussion

3.1. Characterization of defects by (C)DB PAS

3.1.1. DB results after room temperature Fe ion irradiation

Fig. 2a and b display the S and W parameters as a function of incident positron energy for the model alloy and the ODS1 steel after the Fe^+ irradiation at RT, together with the values measured for reference samples of the unirradiated alloys and well annealed pure Fe. The S-parameter of the unirradiated well-annealed model alloy is very similar to the S-parameter of pure Fe. Since the bulk values of S-parameter (as well as W-parameter, Fig. 2b) are almost equal in both samples DB momentum curves seem to be not sensitive to chromium content of the alloys. The S and W-parameters of the unirradiated ODS1 alloy show profiles only slightly increasing and decreasing towards the bulk. The slight slope might be interpreted as a small concentration profile of open-volume positron traps which could stem from the sample preparation. In the bulk, the S-parameter for the ODS sample lies higher than for the well annealed Fe14Cr alloy. This result is similar to the S-depth profiles reported for other commercial ODS steels [31]. It also agrees with positron lifetime measurements, as the same unirradiated ODS materials have a higher positron lifetime of 200 ps while for the bulk of pure, defect-free Fe and Fe14Cr that value is ~106–108 ps and ~109 ps, respectively [32–34]. For positron energies <10 keV, the S-parameters of the model alloy and pure Fe lie above the ones for the ODS sample. It is known that in materials with low number of defects, positron diffusion lengths are longer so more positrons could diffuse back and annihilate near the surface, giving rise to the S-parameter associated with surface annihilation.

Results of the PAS DB measurements for all irradiated alloys show an increase of the S-parameter values in the entire positron energy range. This means that the fraction of positrons annihilating with low momentum electrons has increased, indicating the presence of open volume defects created by the irradiation. The S-parameter profiles of all irradiated samples exhibit a wide maximum region located around 4–22 keV. In Fig. 3 the implantation profiles of positrons for different positron energies have been calculated for an Fe14Cr alloy, according to the Makhovian distribution [35–37]. The obtained profiles indicate the spatial distributions of positrons in the sample after slowing down and thermalization, just before diffusion takes place. As it can be seen, the implantation range of positrons increases with increasing energy. The mean range for 12–14 keV positrons corresponds to implantation depths of 270–350 nm. These values agree very well with the Bragg peak of the Fe^+ irradiation calculated by SRIM (damage profile shown in Fig. 1a) that is estimated to be around 300 nm. In Fig. 1a it is seen that the irradiation induced damage extends up to 600 nm. Therefore, at positron energies higher than 20 keV, the fraction of positrons implanted deeper than 600 nm will become predominant. The increasing contribution from the unirradiated layers is reflected in the S-parameter values that start to decrease towards the bulk value for energies >20 keV. In any case at the highest positron energies there is still an observable influence of damaged layers, due to the smearing of the positron implantation profile. Due to the broadening of the implantation profile of higher energy positrons (Fig. 3), the S-parameter value in the bulk region for the irradiated sample will have some contribution of the shallower, more damaged region [38]. The difference between the S-parameter in the zone of maximum damage post irradiation with respect to the bulk value of an unirradiated sample is ~18% for Fe14Cr and ~6% for the ODS alloy. The much higher S-parameter values obtained in the model alloy indicate a higher concentration and/or larger vacancy clusters forming under the irradiation. The lower increase in the ODS alloys reflects the impact that Y rich nanoparticles, alongside with other sources of vacancy traps (grain boundaries, dislocations, precipitates, etc.) have on reducing the irradiation damage.

3.1.2. DB results after room temperature He ion irradiation

The model alloy and the ODS1 steel were irradiated with 50 keV He^+ ions at RT to 8000 appm. Fig. 2 shows the DB S and W line parameters as a function of the positron incident energy, for both alloys. As it is shown in Fig. 2a, an increase of the S-parameter is observed for both materials, the reverse happening in W-parameter (Fig. 2b). As expected, the effect of the He^+ irradiation is

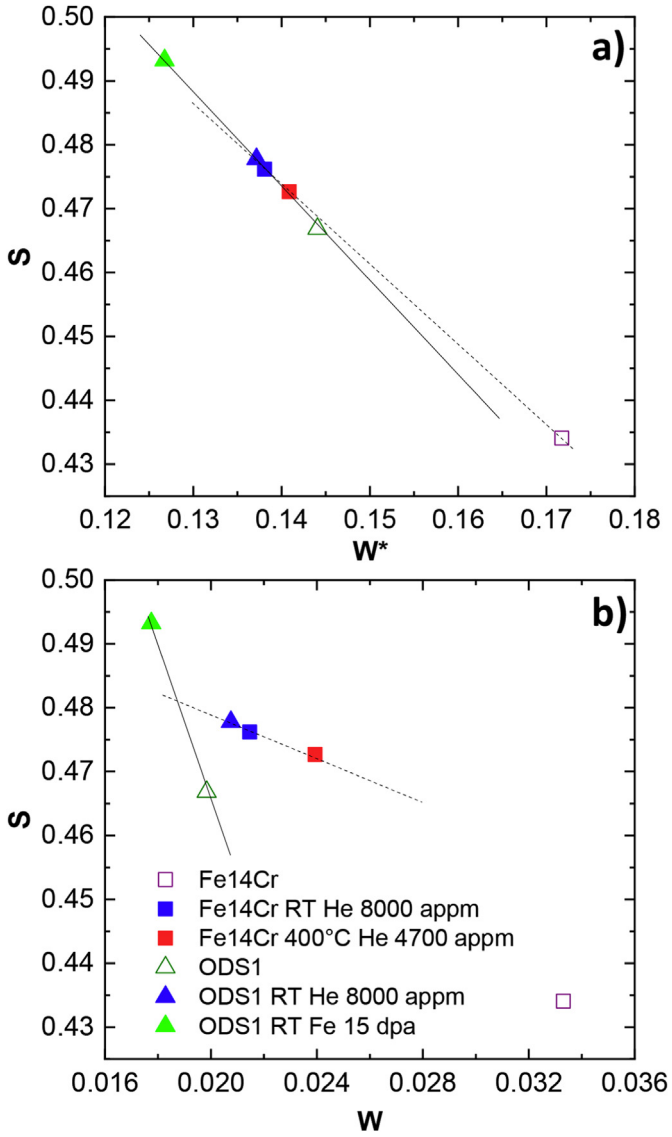

Fig. 5. a) S–W* correlation (where W* corresponds to (7-12) × 10^{-3} m_0c) and b) S–W correlation (where W corresponds to (12–20) × 10^{-3} m_0c) from CDB measurements.

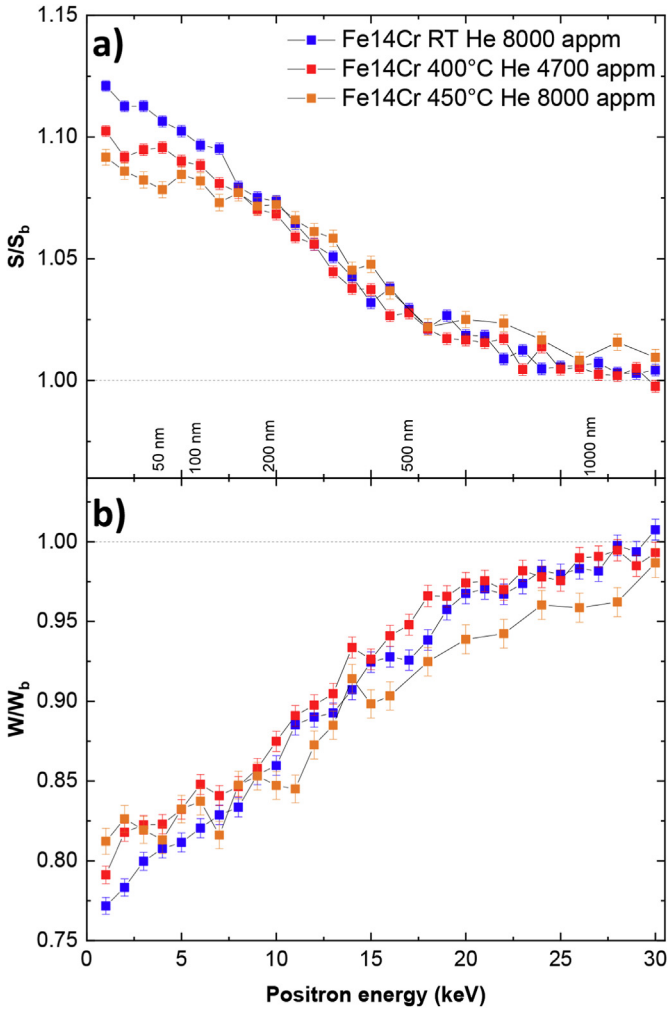

Fig. 6. a) S-parameter and b) W-parameter of the He^+ irradiated Fe14Cr model alloy relative to unirradiated bulk values.

weaker than the changes induced by the Fe^+ irradiations due not only to the much smaller amount of open-volume defects being created but also to the presence of helium atoms in the defects which reduces the positron trapping rate [39,40].

In the irradiated Fe14Cr alloy, there is an increase of the S-parameter in the range of 2–22 keV with respect to the unirradiated sample. However, it does not show a clear maximum and follows the surface-bulk trend of the unirradiated one. This increase of S-parameter, measured at 7 keV, is ~9.5%. At energies higher than 22 keV there are no differences between the irradiated and the unirradiated samples. The Bragg peak for this irradiation is calculated by SRIM to be ~160 nm, and the damage done by He^+ is 0.5 dpa, therefore there are less irradiation induced defects and they are closer to the surface, as compared to the previously discussed Fe^+ irradiations. The S-parameter characteristic of helium bubbles would also be smaller than the value corresponding to empty voids.

Post-irradiation increase of the S-parameter for the ODS1 steel is ~3.3% in the zone of maximum damage. Veternikova et al. obtained an increase of ~7% in the commercial ferritic ODS steel MA 957 (13.7% Cr content) after He irradiation with much higher dose and ion energy [41]. As in the Fe^+ irradiation, the difference with respect to the unirradiated sample is smaller in the ODS steel than in the model alloy, so it appears that Y rich nanoparticles act as recombination sites for irradiation-induced vacancies and implanted He atoms, thus inhibiting growth of vacancy clusters, which would lead to a rise of the S-parameter.

3.1.3. CDB results

CDB profiles were obtained for the ODS1 steel Fe^+ irradiated at RT, Fe14Cr and the ODS1 samples He^+ irradiated at RT, and for the Fe14Cr alloy He^+ irradiated at 400 °C, as well as for their unirradiated counterparts. For the unirradiated samples the profiles were obtained at positron energy of 30 keV to probe the bulk, while for the Fe^+ and He^+ irradiated samples the CDB measurements were done at 18 keV and 7 keV, respectively.

CDB ratio profiles with respect to pure annealed Fe are shown in Fig. 4a. The unirradiated CDB curve for the model alloy is similar to the reference pure Fe, indicating a well annealed sample with little to no open volume defects. The high momentum part of the CDB curve for the unirradiated ODS sample shows a local minimum at ~17 × 10^{-3} m_0c followed by a broad peak centred at ~30 × 10^{-3} m_0c, very similar to the ratio curve of yttrium, which would point to positrons being annihilated in the presence of mainly Y rich

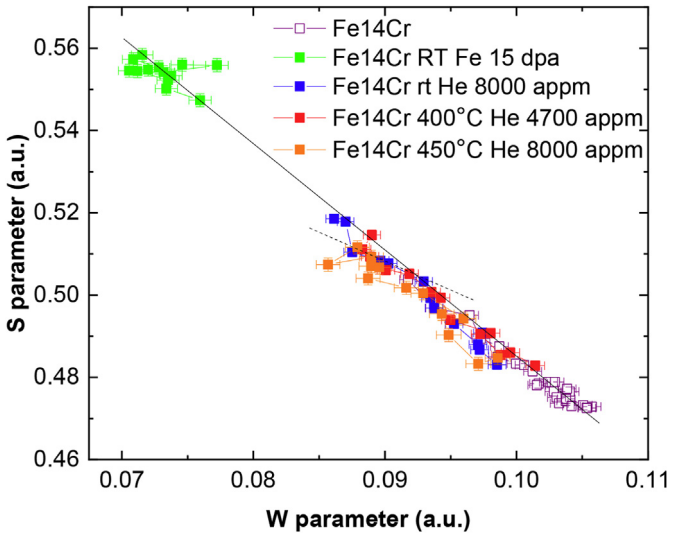

Fig. 7. S–W correlation for unirradiated and irradiated Fe14Cr obtained from DB measurements at incident positron energies in the ranges 6–30 keV (unirradiated) and 6–18 keV (irradiated).

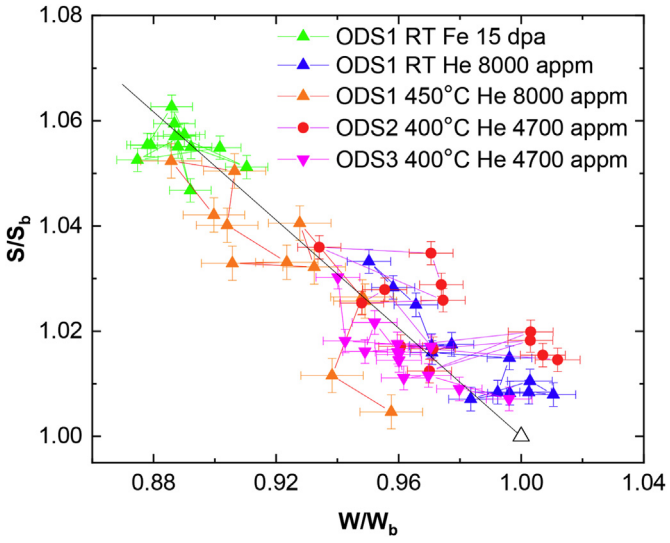

Fig. 9. Normalised S–W correlation for irradiated ODS steels obtained from the single DB measurements at incident positron energies in the 6–18 keV range.

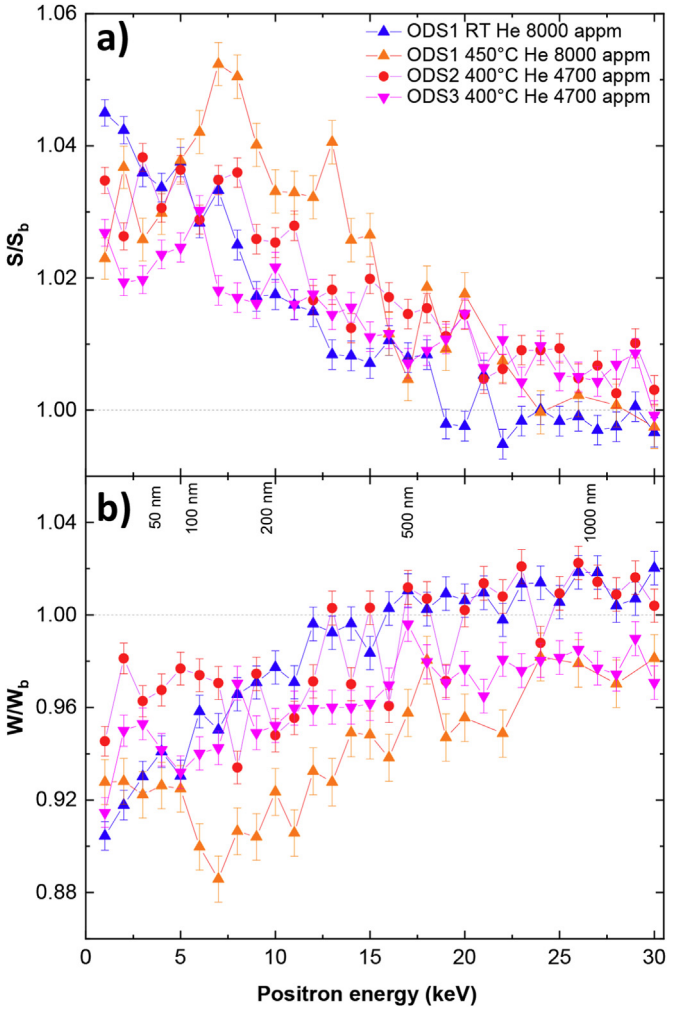

Fig. 8. a) S parameter and b) W parameter of all the He^+ irradiated ODS samples relative to unirradiated bulk values.

positron traps, in agreement with previous publications on ODS steels [42,43].

The lower momentum ($p_L < 5 \times 10^{-3}$ m_0c) portions of the CDB curve for the Fe^+ irradiated ODS sample is lying higher than the one for the non-irradiated suggesting an increase in number/size of the open volume defects. The shape of the higher momentum region of the Fe^+ irradiated ODS sample remained similar to its unirradiated counterpart, indicating that the chemical surrounding of the annihilation site does not change after the irradiation. This can be better intuited in Fig. 4b, where the CDB ratios profiles of the unirradiated samples with respect to their unirradiated counterparts in the momentum region (0-25) $\times 10^{-3}$ m_0c are depicted. As it can be seen, the ratio profile for $p_L > 5 \times 10^{-3}$ m_0c of the Fe^+ irradiated ODS sample is relatively flat and stays below one for the whole region considered. This is consistent with the existence of more open volume defects than in the unirradiated material (less annihilations with core electrons) without a significant change of the chemical environment of the positron traps.

At low momentum, the CDB ratio curve to pure iron (Fig. 4a) of the He^+ irradiated Fe14Cr sample at RT lies higher than for its unirradiated counterpart reflecting open volume defects created by the He ions. For higher momentum values, the profile of the CDB curve of the Fe14Cr He^+ irradiated sample has a local minimum around $15 \times 10^{-3} m_0c$ and a local maximum around $22 \times 10^{-3} m_0c$. The CDB ratios to the unirradiated samples depicted in Fig. 4b show that the behaviour of the CDB curve of the He^+ irradiated Fe14Cr at RT is slightly different from what Anwand et al. observed for a model Fe14Cr alloy irradiated with Fe^+ at −80 °C, also shown in Fig. 4b [44]. This would point to a change in the chemical environment of open-volume traps due to the He^+ irradiation, possibly due to the creation of He-vacancy complexes. Theoretical calculations of DB profiles of He-vacancy complexes in bcc iron have been performed by Sabelová et al. [45,46]. The calculated DB profiles show a distinctive He signal in the region $5–12 \times 10^{-3} m_0c$, with a peak in the CDB ratio profiles to pure Fe > 1 that is absent in the curves calculated for single vacancies and empty vacancy clusters. They also show a very good correlation with experimental measurements of CDB ratio profiles to unirradiated samples in a He^+ implanted Fe12Cr alloy and a spallation irradiated Eurofer97 steel. However, this effect is not evident in the He^+ irradiated Fe14Cr ratio curve shown in Fig. 4b, possibly due to the lower fluences and

energies of the irradiations carried out in this work which would generate less damage, less He concentration and shallower implantation profiles.

CDB profile for He^+ irradiated Fe14Cr model alloy at 400 °C is also shown in Fig. 4a. In the low momentum region, CDB curve of the irradiated sample shows an increase in open volume defects due to the irradiation. In the higher momentum region, the profile of the irradiated Fe14Cr model alloy shows a similar local minimum to the one for the Fe14Cr alloy irradiated with He^+ at RT although less pronounced. However, there is a clear shift in the local maximum position, being much closer to the unirradiated Fe14Cr alloy than in the case of the RT irradiation. The ratio profile in Fig. 4b also shows that the difference with respect to the Fe^+ irradiated Fe14Cr alloy in the higher momentum region becomes much more evident than in the case of the sample He^+ irradiated at RT.

In the case of the He^+ irradiated ODS sample at RT, the CDB ratio profile to pure iron undergoes a change with respect to its unirradiated profile – its local minimum is slightly shifted from $17 \times 10^{-3} m_0c$ to $15 \times 10^{-3} m_0c$ and it has a new local maximum at $22 \times 10^{-3} m_0c$. Fig. 4a shows that the CDB profiles of the two He^+ irradiated samples at RT are almost identical indicating a similar chemical environment. This would imply that the positron traps in the ODS1 steel after this He^+ irradiation are not associated with the nanoparticles being most probably He-vacancy complexes mainly located in the ferritic matrix. The corresponding CDB ratio to the unirradiated ODS sample shown in Fig. 4b also shows a significant change with respect to the Fe^+ irradiated ODS sample. Although the He signal in the $5–12 \times 10^{-3} m_0c$ cannot be detected, a peak appears for higher momentum regions.

The correlation between the annihilation parameters S and W can be used to discriminate between different positron traps. Following [46] three lineshape parameters have been obtained from the CDB measurements; S in the low momentum region $(0–2.5) \times 10^{-3}$ m_0c, W in the higher momentum region $(12–20) \times 10^{-3}$ m_0c, and W* in the region corresponding to the He fingerprint $(7\text{-}12) \times 10^{-3}$ m_0c. Fig. 5a and b depict the S–W* and S–W plots for all CDB measurements realised. From the S–W* plot very little information can be extracted; all the data lie almost in one single line, with higher S values corresponding to higher concentration or growth of open volume defects, but no more visible differences between the defects produced by the He^+ irradiations and the Fe^+ irradiations. This would again indicate that the defect structure generated by the He^+ irradiation

ns carried out in this work is below the detection limit of the He signal in this region. However, in the case of the S–W plot (Fig. 5b) two distinct trends can be observed: the S–W value from the He^+ irradiation at RT in the ODS1 steel does not lie in the same line that connects the Fe^+ irradiated value with the unirradiated ODS1, but it fits with the line connecting the two values obtained for the He^+ irradiated Fe14Cr alloy. On the other hand, it is not possible to fit these two data with the unirradiated Fe14Cr value. This behaviour could be evidence of a different chemical environment surrounding the defects in the He^+ irradiated Fe14Cr alloy, being of similar nature than the defects detected in the He^+ irradiated ODS1 steel. A similar change of slope correlated with the presence of He is observed in theoretical S–W* plots for pure iron [47]. The results obtained agree with CDB studies performed in proton and neutron irradiated ferritic martensitic steels where a change in the slope of the S–W plots is evidenced when gas atoms are produced during the irradiation [48].

3.1.4. DB results after high temperature He ion irradiations

The model Fe14Cr alloy and ODS1 steel were irradiated at 450 °C to a maximum He concentration of 8000 appm. Another sample of the Fe14Cr model alloy, the ODS2 and ODS3 steels were irradiated at 400 °C to a maximum He concentration of 4700 appm.

DB S and W profiles of the He^+ irradiated Fe14Cr model alloy are shown in Fig. 6 normalised to bulk values. The S-parameters of the Fe14Cr sample irradiated with He^+ at 400 °C and 450 °C are very similar and show a similar trend as the S-parameter of the Fe14Cr sample irradiated at RT (Fig. 2). The increase in S-parameter for 400 °C and 450 °C irradiations, in the zone of maximum damage (Bragg peak calculated to be ~160 nm), are 8% and 7.3% respectively which is comparable to the change in the case of the RT irradiation (9.5%). It should be pointed out that the dose in the case of He^+ irradiation at 450 °C is double compared to the case of 400 °C irradiation, hence it appears that in the zone of maximum damage either a saturation of positron traps or some annealing is taking place at 450 °C. The S–W plots for all irradiated Fe14Cr samples obtained from the single DB measurements are depicted in Fig. 7 in the range 6–18 keV together with the values for unirradiated Fe14Cr in the range 6–30 keV. Although more noisy than the S–W plots obtained from CDB measurements, some changes can be observed. As it can be seen, the data corresponding to the He^+ irradiations that have the highest S values (which would indicate an increase or growth of vacancy-type defects) show a small deviation

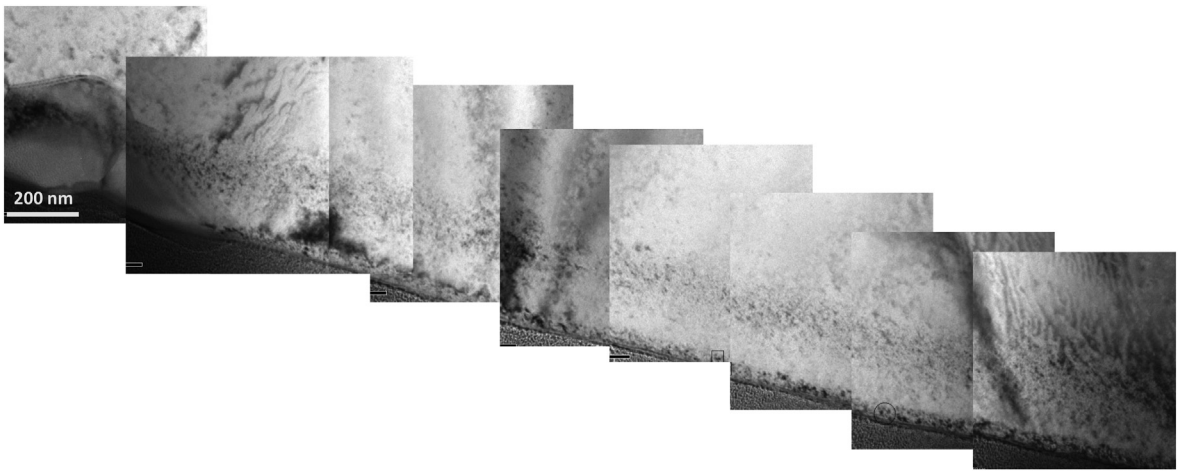

Fig. 10. BF-TEM image of the He^+ irradiated Fe14Cr alloy at 400 °C showing a defect fringe ranging between 150 and 240 nm of depth. The darker bottom of the images corresponds to the Pt layer deposited on the sample surface in the FIB process.

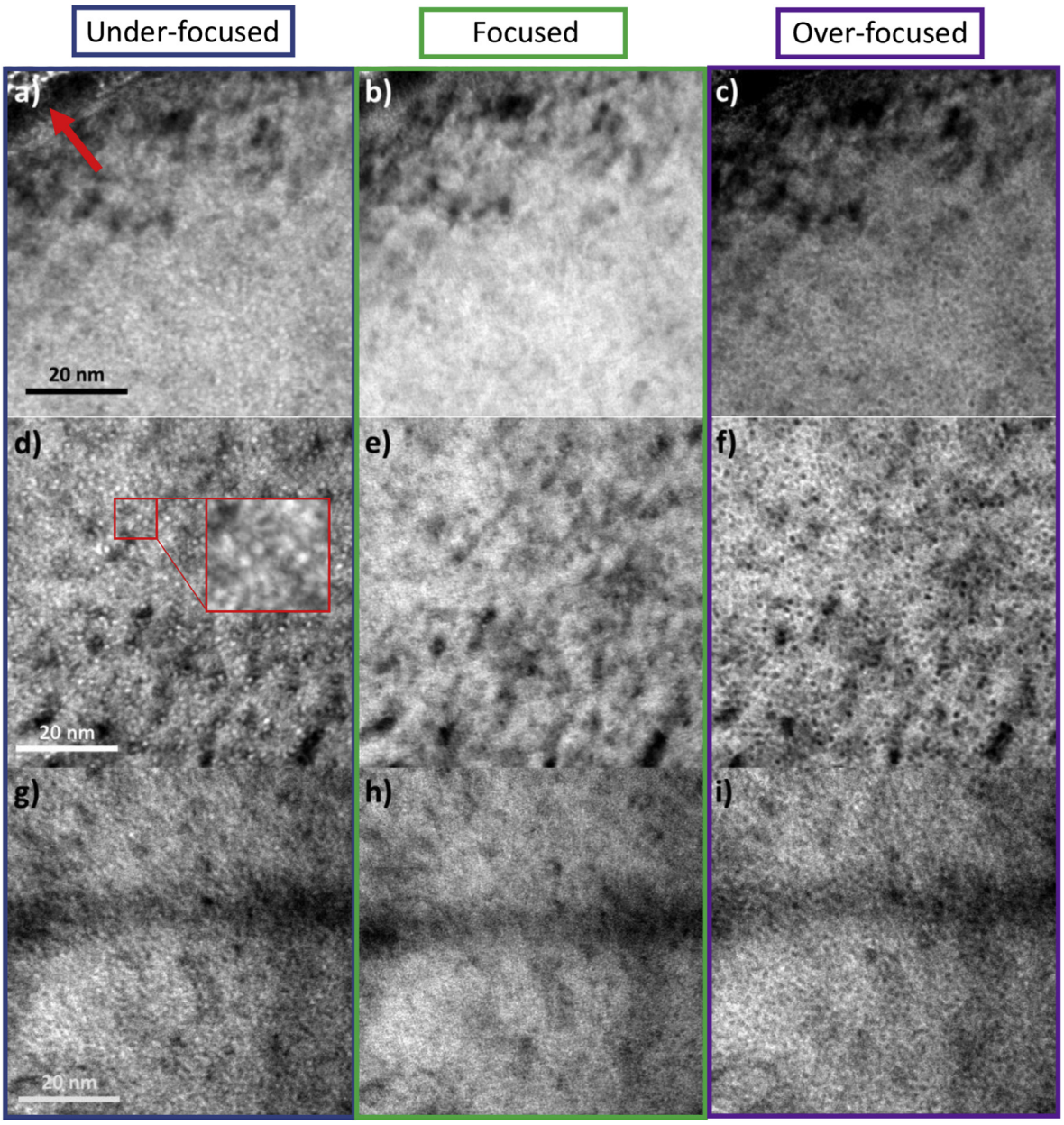

Fig. 11. Through-focal series of three regions in the He^+ irradiated Fe14Cr alloy at 400 °C: a)-c) a region outside the bubble fringe towards the surface at ~100 nm from it (Pt layer marked by an arrow) (thickness 74 ± 15 nm); d)-f) a region inside the bubble fringe at ~200 nm from the surface (inset showing magnified bubbles) (thickness 160 ± 30 nm) and g)-i) a region outside the bubble fringe deeper in the sample at ~300 nm from the surface (thickness 150 ± 30 nm).

from the line connecting the unirradiated and Fe^+ irradiated values, that could be due to the presence of He-vacancy complexes, being more evident in the He^+ irradiation performed at highest dose and temperature.

Fig. 8 shows PAS DB results of all the ODS samples He^+ irradiated relative to their unirradiated state. The S-parameter profiles for ODS1 after He^+ irradiations at 450 °C and RT, both to the same dose (8000 appm maximum He concentration), are presented together with the profiles for the ODS2 and ODS3 steels irradiated at 400 °C to a maximum He concentration of 4700 appm. Unlike the previously discussed model alloy, the ODS1 steel shows the effect of the temperature of irradiation on the creation of new traps. The S-parameter of the sample irradiated at 450 °C presents a more pronounced maximum at ~7 keV, being its value 5.2% higher than bulk value. For the RT irradiation that increase was 3.3%. It has to be taken into account that while the Fe14Cr alloy was almost defect free in the unirradiated state, the ODS steel already contained a high density of nanoparticles, grain boundaries and dislocations that have been proven to trap and stabilise a significant population of vacancy clusters [32]. These microstructural features present in the ODS alloys could therefore be also acting as effective He and vacancy sinks coming from the irradiation.

The increase of the S-parameter in the ODS2 and ODS3 steels is very similar, ~3.5% and ~2.8% respectively, which are lower than in the case of the ODS1 steel. The different behaviour as compared to the model alloy would imply that there is a transition in the irradiation induced defects in the ODS steels when increasing dose and temperature in the ranges 6×10^{15}–10^{16} ions/cm^2 and 400–450 °C. Fig. 9 shows the relative S–W plots for all irradiated ODS samples obtained from the single DB in the range 6–18 keV. However, data

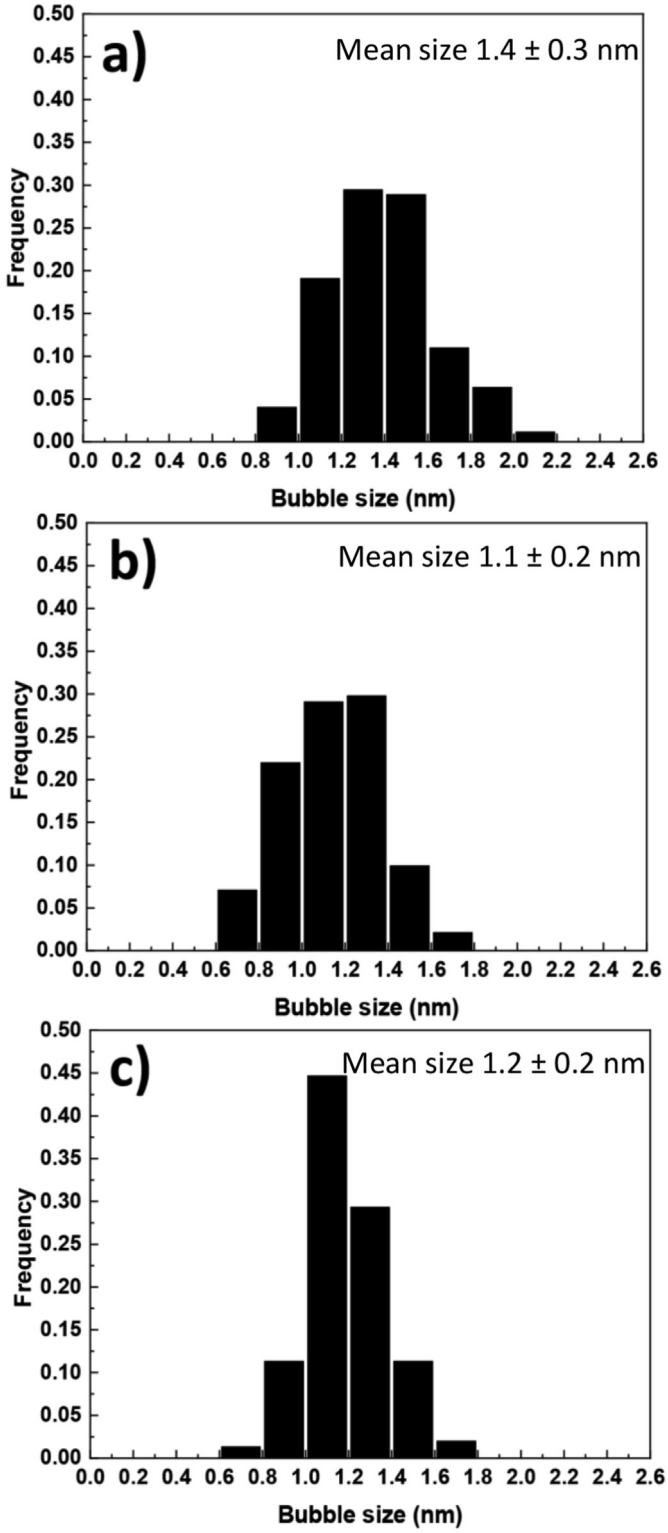

Fig. 12. Bubble size distribution in the He^+ irradiated alloys at 400 °C. a) Fe14Cr, b) ODS2 and c) ODS3.

show too much scatter to identify clearly any change in the S–W correlations that could be attributed to different type of defects. Future PAS experiments regarding characterization of CDB profiles from the He^+ irradiated ODS steels at 400–450 °C will help to clarify the changes observed.

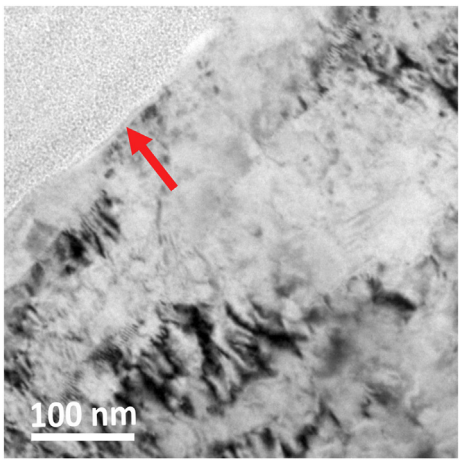

Fig. 13. BF-TEM image of the ODS2 steel irradiated with He^+ at 400 °C. The arrow marks the Pt layer deposited during the sample preparation.

3.2. TEM characterization of bubbles induced by He ion irradiations at 400 °C

3.2.1. Fe14Cr

A series of low magnification general images of the Fe14Cr model alloy irradiated at 400 °C (Fig. 10) show a clear defect fringe at the depth that coincides with the location of the maximum estimated damage. The Bragg peak calculated by SRIM is located at ~160 nm from the surface and the area of the maximum concentration of He is at ~200 nm. No visible bubbles were detected at these magnifications. The presence of small He bubbles was investigated at higher magnifications in five regions, three of which were inside the fringe, one region closer to the surface and one deeper into the sample (see Fig. 11). The through-focal series done confirmed the existence of a homogeneous distribution of small bubbles inside the fringe (Fig. 11 d to f). In the under-focused images bubbles appear with bright contrast, while in the over-focused they appear with a dark one. In the region deeper into the sample (~300 nm) there were no visible bubbles. Their number density was estimated by counting the number of bubbles in both over-focused and under-focused images. The final number was then obtained by calculating the mean value. The three regions located ~200 nm have bubble number densities ranging from $(2.8 \pm 0.8) \times 10^{23}$ m^{-3} to $(5.7 \pm 1.1) \times 10^{23}$ m^{-3}. It has to be noted that this type of measurements has some inherent imprecision. Small changes in BF imaging conditions could lead to slight changes in the number of visible bubbles. Their size distribution is shown in Fig. 12a. The mean size of the measured bubbles is 1.4 ± 0.3 nm, with all of them being smaller than 2.5 nm. These results are in general agreement with previous reported sizes and number densities of He bubbles measured in an Fe14Cr alloy after He^+ irradiation at 500 °C up to 6.5×10^{16} ions/cm^2 where the mean size was 2.8 nm and the number density 7.3×10^{23} m^{-3} respectively [49]. At this irradiation temperature there appears to be diffusion of He towards the surface as in the region 100 nm away from the surface there is a homogeneous distribution of bubbles. Their mean size is similar to the one measured in the regions in the vicinity of maximum concentration of He, being 1.2 ± 0.2 nm while the number density is lower, $(3 \pm 2) \times 10^{23}$ m^{-3}.

3.2.2. ODS2

Fig. 13 shows the microstructure of the ODS2 steel after the irradiation. No clear defect fringe was observed in this case. This could be due to the much more complex microstructure present in

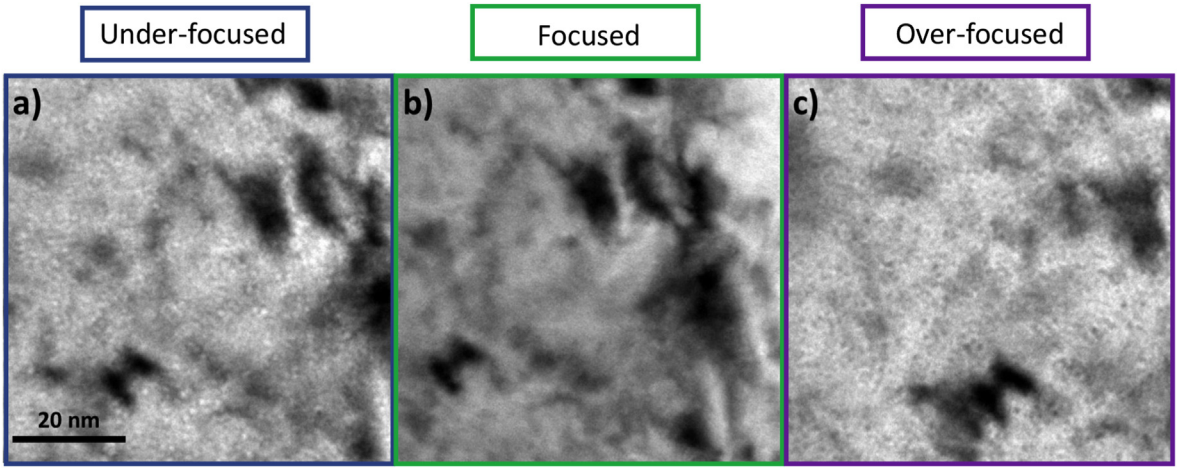

Fig. 14. Through-focal series of a region at the highest He concentration in the He^+ irradiated ODS2 steel at 400 °C: a) under-focused image by 500 nm, b) in-focus image and c) over-focused image by 500 nm. The thickness of the region is 34 ± 7 nm.

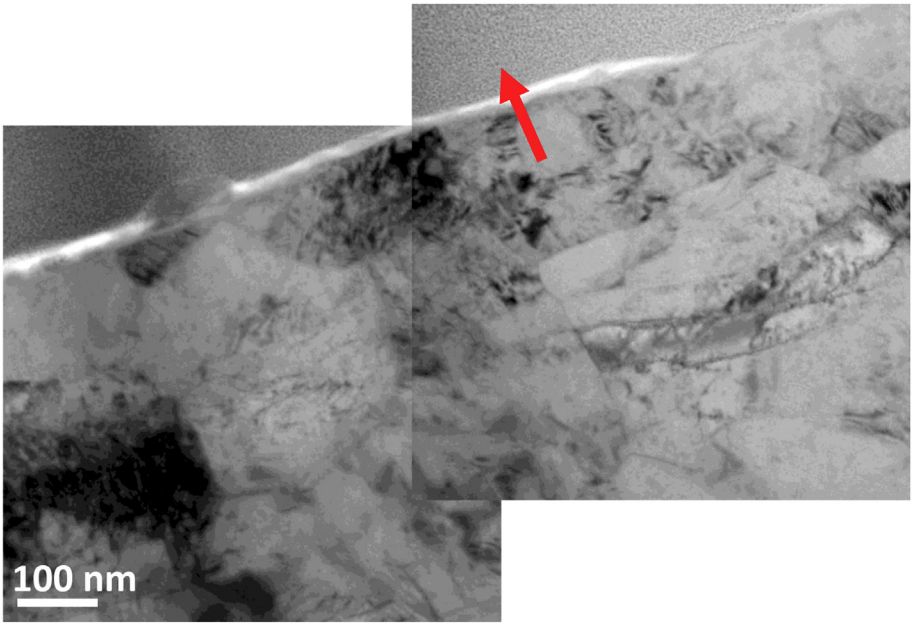

Fig. 15. BF-TEM image of the ODS3 steel irradiated with He^+ at 400 °C. The arrow marks the Pt layer deposited during the sample preparation.

the ODS steel, although no further orientation studies were accomplished. The presence of irradiation induced bubbles was investigated in six regions located in the vicinity of the maximum He concentration (~200 nm from the surface). Through-focal series of bubbles induced by the 400 °C He^+ irradiation are shown in Fig. 14. Bubble number densities measured in two regions were $(10 \pm 2) \times 10^{23}$ m^{-3} and $(11 \pm 2) \times 10^{23}$ m^{-3}. The mean size of bubbles was 1.1 ± 0.2 nm and the maximum size measured was below 2 nm. The bubble size distribution is shown in Fig. 12b. These results are in agreement with what was previously observed by Edmondson et al. in a ferritic ODS steel irradiated with He^+ at 400 °C where the mean size of bubbles was 2 ± 1 nm [50]. These densities are higher than what was observed for the previously discussed Fe14Cr sample at the same depth, while the sizes of bubbles are slightly smaller. There was no clear association between bubbles and nanoparticles in the studied areas, appearing homogeneously dispersed within the matrix. This is supported by a previous study done for a nanostructured ferritic alloy of similar composition, irradiated with He^+ at 400 °C, in which it was found that ~94% of bubbles with mean size of 1.0 ± 0.6 nm were located in the ferritic matrix of the sample [51].

3.2.3. ODS3

In this sample, similarly to the previously discussed ODS2 steel, there was no visible defect fringe induced by this irradiation, as can be seen in Fig. 15. The through focal series of regions nearby the area of maximum He concentration are shown in Fig. 16. Five different regions were studied, and it can be observed that in the region deeper into the sample (Fig. 16 g-i) there are few visible He bubbles.

Number densities measured in four different regions of the sample ~200 nm depth ranged from (3.8 ± 1.3) to $(12 \pm 3) \times 10^{23}$ m^{-3}. Towards the surface of the sample, the density is also very high, being $(10 \pm 2) \times 10^{23}$ m^{-3}. Most of the bubbles are

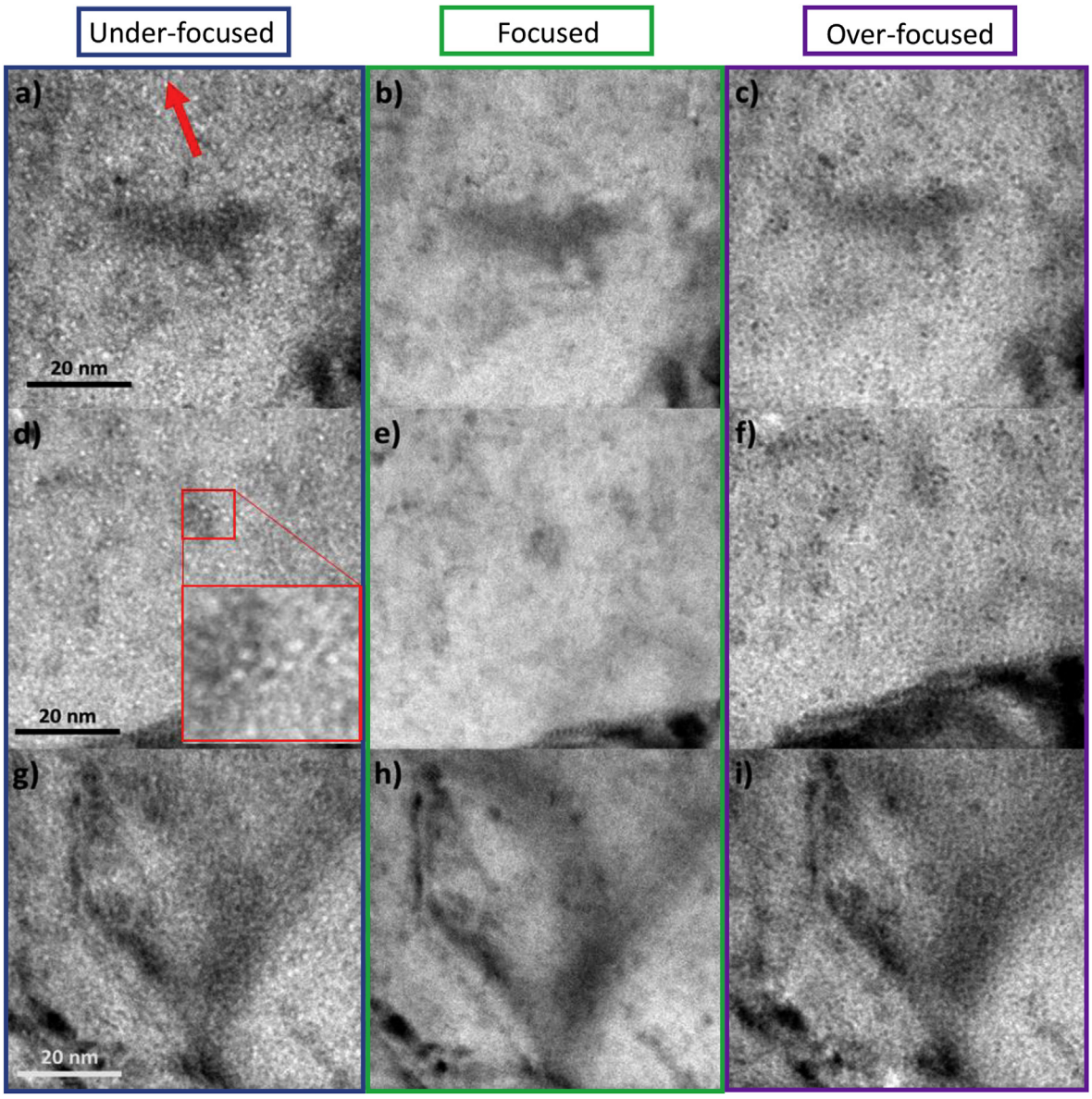

Fig. 16. Through-focal series of three regions in the He^+ irradiated ODS3 steel at 400 °C: a)-c) a region outside the bubble fringe towards the surface at ~100 nm (the arrow is marking the direction towards the surface) (thickness 60 ± 12 nm); d)-f) a region inside the bubble fringe at ~200 nm (inset showing bubbles attached to a nanoparticle) (thickness 61 ± 12 nm) and g)-i) a region outside the bubble fringe deeper in the sample at ~300 nm from the surface (thickness 110 ± 20 nm).

Table 2
Mean sizes and mean number densities of irradiation induced bubbles created by He^+ irradiation at 400 °C.

Sample	Mean bubble size (nm)	Mean number density of bubbles ($\times 10^{23}$ m^{-3})
Fe14Cr	1.4 ± 0.3	4 ± 1
ODS2	1.1 ± 0.2	10 ± 2
ODS3	1.2 ± 0.2	8 ± 2

located in the matrix although some of them can also be seen attached to nanoparticles (see Fig. 16 d). The bubble size distribution is shown in Fig. 12c, where the mean size is 1.2 ± 0.2 nm, and the maximum diameter observed is below 2 nm, similar to the previously described ODS2 steel, regardless of their different production processes. This agrees with the PAS results for both ODS2 and ODS3 steels after the 400 °C He^+ irradiation, where S-parameters of both irradiated samples are very similar.

Table 2 shows mean sizes and mean number densities (measured in the area of estimated maximum concentration of He) of the three investigated alloys irradiated with He^+ at 400 °C up to 6.5×10^{15} ions/cm^2. The sizes of bubbles visible by TEM are similar for the two ODS steels and smaller than the ones found for the model alloy. Bubble number densities are higher for the two ODS steels than for the model alloy, although the order of magnitude remains the same. This suggests that ODS steels are effective in reducing the coarsening of bubbles created under these irradiation conditions. These results imply that although few nanoparticles

were observed attached to bubbles, their presence (together with the overall complex microstructure of ODS steels) modifies the evolution of vacancies and He-vacancy complexes generated by the irradiation, preventing significant bubble growth.

4. Conclusions

The main findings of the present study are summarised as follows:

- PAS has been applied to characterise the defects induced by Fe^+ irradiation at room temperature on the model alloy and the ODS1 steel. For all the samples, the S-parameter value was higher after irradiation, indicating an increase of the concentration of vacancies or the size of the vacancy clusters under these irradiation conditions. The DB measurements showed that the S-parameter increase for the ODS alloy after irradiation is lower than in the case of the model alloy, and the CDB profile of the irradiated ODS1 steel suggests the existence of traps associated with the Y signal. These results confirm the role of the Y rich nanoparticles, by acting as vacancy sinks or pinning them, in hindering the creation of bigger vacancy clusters.
- The effect of He^+ irradiation at room temperature is weaker as compared to the Fe^+ irradiation. The change is more obvious in the model alloy. CDB profiles point to some irradiation induced changes. In the case of the Fe14Cr alloy, it appears that the chemical environment of open-volume traps has changed due to the He^+ irradiation, possibly due to creation of He-vacancy complexes. In the case of the irradiated ODS1 sample, the CDB profile undergoes a change with respect to its unirradiated profile and becomes identical to the profile of the irradiated Fe14Cr sample suggesting that in the ODS1 after irradiation positron traps are not associated with nanoparticles but are in the ferritic matrix.
- All samples were irradiated at high temperatures with He^+ ions. S-parameters of the Fe14Cr sample irradiated with He^+ at 400 °C and 450 °C are very similar in the zone of maximum damage, despite the dose in the case of He^+ irradiation at 450 °C being double than in the case of 400 °C irradiation. It appears that there is a saturation of positron traps or some annealing is happening at 450 °C. These profiles are also similar to the S-parameter profile after RT He^+ irradiation, showing almost no effect of the temperature of irradiation. This is not the case for the ODS1 sample irradiated with He^+ at 450 °C, where a clear increase of the S-parameter is observed in the zone of maximum damage. S-parameter profiles of both the ODS2 and ODS3 samples are very similar before and after He^+ irradiation at 400 °C. This would indicate a transition in the irradiation induced defects in ODS steels when increasing dose and temperature, although further experiments are required to confirm it.
- TEM investigation of irradiation induced bubbles was done for the model alloy, ODS2 and ODS3 samples irradiated with He^+ at 400 °C. In all three samples, small bubbles (<2.5 nm) were observed. Bubble sizes are similar for the two ODS steels and smaller than the ones found for the model alloy, being the visible bubble number densities higher for the two ODS steels. Although the majority of bubbles are observed in the ferritic matrix, ODS steels seem to be effective in reducing the coarsening of bubbles created under these irradiation conditions.

Data availability statement

Data will be made available upon request.

CRediT authorship contribution statement

M. Šćepanović: Investigation, Writing - original draft, Writing - review & editing. **V. de Castro:** Investigation, Writing - original draft, Writing - review & editing, Resources, Supervision. **I. García-Cortés:** Investigation, Resources. **F.J. Sánchez:** Investigation, Resources. **T. Gigl:** Investigation. **C. Hugenschmidt:** Investigation, Resources, Writing - review & editing. **T. Leguey:** Investigation, Writing - original draft, Writing - review & editing, Resources, Supervision.

Acknowledgements

This investigation has been supported by the Ministerio de Economía y Competitividad MINECO (project ENE2015-70300-C3-2-R) and the Comunidad de Madrid through the program TECHNOFUSIÓN-III (S2018/EMT-4437). Slow positron annihilation measurements at NEPOMUC received financial support provided by FRM II (Heinz Maier-Leibnitz Zentrum, Garching, Germany). The authors also acknowledge the support provided by CMAM and CIEMAT facilities and the Centro Nacional de Microscopía Electrónica (Madrid, Spain). Financial support from Spanish MINECO under project ENE2016-76755-R is also acknowledged.

References

[1] H. Ritchie, M. Roser, Energy Production & Changing Energy Sources. https://ourworldindata.org/energy-production-and-changing-energy-sources.
[2] V. Masson-Delmotte, P. Zhai, H.-O. Pörtner, D. Roberts, J. Skea, P.R. Shukla, A. Pirani, W. Moufouma-Okia, C. Péan, R. Pidcock, S. Connors, J.B.R. Matthews, Y. Chen, X. Zhou, M.I. Gomis, E. Lonnoy, T. Maycock, M. Tignor, T. Waterfield, reportGlobal Warming of 1.5°C an IPCC Special Report, n.d. doi:10.1017/CBO9781107415324.
[3] ITER - the Way to New Energy. https://www.iter.org. (Accessed 9 January 2020).
[4] R.L. Klueh, D.R. Harries, High-chromium Ferritic and Martensitic Steels for Nuclear Applications, ASTM International, 2001.
[5] L.K. Mansur, Theory and experimental background on dimensional changes in irradiated alloys, J. Nucl. Mater. 216 (1994) 97–123, https://doi.org/10.1016/0022-3115(94)90009-4.
[6] E.E. Bloom, The challenge of developing structural materials for fusion power systems 263 (2008) 7–17, https://doi.org/10.1016/S0022-3115(98)00352-3.
[7] S.J. Zinkle, L.L. Snead, Designing radiation resistance in materials for fusion energy, Annu. Rev. Mater. Res. 44 (2014) 241–267, https://doi.org/10.1146/annurev-matsci-070813-113627.
[8] S. Ukai, M. Fujiwara, Perspective of ODS alloys application in nuclear environments, J. Nucl. Mater. 307–311 (2002) 749–757, https://doi.org/10.1016/S0022-3115(02)01043-7.
[9] G.R. Odette, M.J. Alinger, B.D. Wirth, Recent developments in irradiation-resistant steels, Annu. Rev. Mater. Res. 38 (2008) 471–503, https://doi.org/10.1146/annurev.matsci.38.060407.130315.
[10] M.J. Alinger, G.R. Odette, D.T. Hoelzer, On the role of alloy composition and processing parameters in nanocluster formation and dispersion strengthening in nanostuctured ferritic alloys, Acta Mater. 57 (2009) 392–406, https://doi.org/10.1016/j.actamat.2008.09.025.
[11] C.A. Williams, P. Unifantowicz, N. Baluc, G.D.W. Smith, E.A. Marquis, The formation and evolution of oxide particles in oxide-dispersion- strengthened ferritic steels during processing, Acta Mater. 61 (2013) 2219–2235, https://doi.org/10.1016/j.actamat.2012.12.042.
[12] G.R. Odette, Recent progress in developing and qualifying nanostructured ferritic alloys for advanced fission and fusion applications, JOM (J. Occup. Med.) 66 (2014) 2427–2441, https://doi.org/10.1007/s11837-014-1207-5.
[13] L. Tan, L.L. Snead, Y. Katoh, Development of new generation reduced activation ferritic-martensitic steels for advanced fusion reactors, J. Nucl. Mater. 478 (2016) 42–49, https://doi.org/10.1016/j.jnucmat.2016.05.037.
[14] K. Morishita, R. Sugano, B.D. Wirth, T. Diaz de la Rubia, Thermal stability of helium–vacancy clusters in iron, Nucl. Instrum. Methods Phys. Res. Sect. B Beam Interact. Mater. Atoms 202 (2003) 76–81, https://doi.org/10.1016/S0168-583X(02)01832-3.
[15] G.S. Was, R.S. Averback, Radiation Damage Using Ion Beams, Elsevier Inc., 2012, https://doi.org/10.1016/B978-0-08-056033-5.00007-0.
[16] Y. Dai, G.R. Odette, T. Yamamoto, The Effects of Helium in Irradiated Structural Alloys, first ed., Elsevier Inc., 2012 https://doi.org/10.1016/B978-0-08-056033-5.00006-9.
[17] P. Spätig, J.-C. Chen, G.R. Odette, Ferritic and tempered martensitic steels. Struct. Alloy. Nucl. Energy Appl., Elsevier, 2019, pp. 485–527, https://doi.org/10.1016/b978-0-12-397046-6.00011-3.

[18] R. Odette, N.J. Cunningham, T. Stan, M.E. Alam, Y. De Carlan, Nano-oxide dispersion-strengthened steels, struct, Alloy. Nucl. Energy Appl. (2019) 529–583, https://doi.org/10.1016/B978-0-12-397046-6.00012-5.
[19] J.P. Wharry, M.J. Swenson, K.H. Yano, A review of the irradiation evolution of dispersed oxide nanoparticles in the b.c.c. Fe-Cr system: current understanding and future directions, J. Nucl. Mater. 486 (2017) 11–20, https://doi.org/10.1016/j.jnucmat.2017.01.009.
[20] L. Malerba, A. Caro, J. Wallenius, Multiscale modelling of radiation damage and phase transformations: the challenge of FeCr alloys, J. Nucl. Mater. 382 (2008) 112–125, https://doi.org/10.1016/j.jnucmat.2008.08.014.
[21] N. Castin, M.I. Pascuet, L. Messina, C. Domain, P. Olsson, R.C. Pasianot, L. Malerba, Advanced atomistic models for radiation damage in Fe-based alloys: contributions and future perspectives from artificial neural networks, Comput. Mater. Sci. 148 (2018) 116–130, https://doi.org/10.1016/J.COMMATSCI.2018.02.025.
[22] G. Monnet, Multiscale modeling of irradiation hardening: application to important nuclear materials, J. Nucl. Mater. 508 (2018) 609–627, https://doi.org/10.1016/J.JNUCMAT.2018.06.020.
[23] P. Trocellier, S. Agarwal, S. Miro, A review on helium mobility in inorganic materials, J. Nucl. Mater. 445 (2014) 128–142, https://doi.org/10.1016/J.JNUCMAT.2013.10.061.
[24] M.A. Auger, V. de Castro, T. Leguey, M.A. Monge, A. Muñoz, R. Pareja, Microstructure and tensile properties of oxide dispersion strengthened Fe–14Cr–0.3Y2O3 and Fe–14Cr–2W–0.3Ti–0.3Y2O3, J. Nucl. Mater. 442 (2013) S142, https://doi.org/10.1016/j.jnucmat.2012.11.001. –S147.
[25] J. Macias Delgado, Microestructura y propiedades mecánicas de aceros de activación reducida endurecidos mediante dispersión de óxidos, PhD Thesis, Universidad Carlos III de Madrid, 2019.
[26] J. Macías-Delgado, T. Leguey, V. de Castro, Effect of hot cross rolling on the microstructure and mechanical properties of an Fe-14Cr ODS ferritic steel, Mater. Sci. Eng. 711 (2018) 448–459, https://doi.org/10.1016/j.msea.2017.11.067.
[27] CMAM Centro de Micro-Análisis de Materiales (accessed June 22, 2019), https://www.cmam.uam.es.
[28] I. García-Cortés, T. Leguey, F.J. Sánchez, A. Maira, A. Moroño, P. Muñoz, M. Scepanovic, J.F. Marco, Study of damage in binary Fe85Cr15 alloys irradiated by ions and the effect of an external magnetic field during irradiation, J. Nucl. Mater. 517 (2019) 138–147, https://doi.org/10.1016/J.JNUCMAT.2019.02.009.
[29] C. Hugenschmidt, C. Piochacz, NEPOMUC: neutron induced positron source Munich, J. Large-Scale Res. Facil. JLSRF. 1 (2015) A22, https://doi.org/10.17815/jlsrf-1-49.
[30] Y. Nagai, Z. Tang, M. Hasegawa, Chemical analysis of precipitates in metallic alloys using coincidence Doppler broadening of positron annihilation radiation, Radiat. Phys. Chem. 58 (2000) 737–742, https://doi.org/10.1016/S0969-806X(00)00250-4.
[31] J.Š. Veterníková, J. Degmová, V. Sabelová, M. Petriska, V. Slugeň, Surface study of radiation damaged oxide dispersion strengthened steels, Appl. Surf. Sci. 312 (2014) 199–202, https://doi.org/10.1016/j.apsusc.2014.02.146.
[32] R. Domínguez-Reyes, M.A. Auger, M.A. Monge, R. Pareja, Positron annihilation study of the vacancy clusters in ODS Fe–14Cr alloys, Philos. Mag. A 97 (2017) 833–850, https://doi.org/10.1080/14786435.2017.1280621.
[33] M. Eldrup, B.N. Singh, Study of defect annealing behaviour in neutron irradiated Cu and Fe using positron annihilation and electrical conductivity, J. Nucl. Mater. 276 (2000) 269–277, https://doi.org/10.1016/S0022-3115(99)00186-5.
[34] J. Chojcan, M. Szuszkiewicz, The Mössbauer effect and positron annihilation studies of Fe-Cr alloys, Phys. Scripta 36 (1987) 820–823, https://doi.org/10.1088/0031-8949/36/5/009.
[35] D. Keeble, U. Brossmann, Positron annihilation studies of materials, Characteriaztion Mater. (2012), https://doi.org/10.1002/0471266965.com110.pub2.
[36] P.J. Schultz, K.G. Lynn, Interaction of positron beams with surfaces, thin films, and interfaces, Rev. Mod. Phys. 60 (1988) 701–779, https://doi.org/10.1103/RevModPhys.60.701.
[37] A. Vehanen, K. Saarinen, P. Hautojärvi, H. Huomo, Profiling multilayer structures with monoenergetic positrons, Phys. Rev. B 35 (1987) 4606–4610, https://doi.org/10.1103/PhysRevB.35.4606.
[38] S. Saini, R. Menon, S.K. Sharma, A.P. Srivastava, S. Mukherjee, P.Y. Nabhiraj, P.K. Pujari, D. Srivastava, G.K. Dey, Ar irradiated Cr rich Ni alloy studied using positron annihilation spectroscopy, J. Nucl. Mater. 479 (2016) 279–286, https://doi.org/10.1016/j.jnucmat.2016.07.016.
[39] T. Troev, E. Popov, P. Staikov, N. Nankov, Positron lifetime studies of defects in α-Fe containing helium, Phys. Status Solidi Curr. Top. Solid State Phys. 6 (2009) 2373–2375, https://doi.org/10.1002/pssc.200982129.
[40] A.B. Walker, K.O. Jensen, J. Szymański, D. Neilson, Positron-surface sticking rates, Phys. Rev. B 46 (1992) 1687–1696, https://doi.org/10.1103/PhysRevB.46.1687.
[41] J. Simeg Veternikova, V. Slugen, S. Sojak, M. Skarba, E. Korhonen, S. Stancek, J. Degmova, V. Sabelova, I. Bartosova, Application of slow positron beam for study of commercial oxide-dispersion-strengthened steels, J. Nucl. Mater. 450 (2014) 99–103, https://doi.org/10.1016/J.JNUCMAT.2013.12.003.
[42] Y. Ortega, V. De Castro, M.A. Monge, A. Muñoz, T. Leguey, R. Pareja, Positron Annihilation Characteristics of ODS and Non-ODS EUROFER isochronally annealed, vol. 376, 2008, pp. 222–228, https://doi.org/10.1016/j.jnucmat.2008.03.005.
[43] I. Bartošová, J. Čížek, F. Lukáč, V. Slugeň, Vickers hardness and positron annihilation study of Eurofer97 and ODS Eurofer, Acta Phys. Pol., A 125 (2014) 702–705, https://doi.org/10.12693/APhysPolA.125.702.
[44] W. Anwand, T. Leguey, M. Scepanovic, F.J. Sanchez, I. García-Cortés, A. Wagner, Fe^{+}implantation Induced Damage in Oxide Dispersion Strengthened Steels Investigated by Doppler Broadening Spectroscopy, 2016, https://doi.org/10.4028/DDF.373.113.
[45] V. Sabelová, V. Kršjak, J. Kuriplach, M. Petriska, V. Slugeň, J. Šimeg Veterníková, Characterization of helium implanted Fe-Cr alloys by means of positron annihilation methods, J. Nucl. Mater. 450 (2014) 54–58, https://doi.org/10.1016/j.jnucmat.2013.10.039.
[46] V. Sabelová, V. Kršjak, J. Kuriplach, Y. Dai, V. Slugeň, Coincidence Doppler broadening study of Eurofer 97 irradiated in spallation environment, J. Nucl. Mater. 458 (2015) 350–354, https://doi.org/10.1016/J.JNUCMAT.2014.12.053.
[47] V. Krsjak, J. Kuriplach, T. Shen, V. Sabelova, K. Sato, Y. Dai, Helium behavior in ferritic/martensitic steels irradiated in spallation target, J. Nucl. Mater. 456 (2015) 382–388, https://doi.org/10.1016/J.JNUCMAT.2014.10.014.
[48] K. Sato, S. Kawamoto, K. Ikemura, V. Krsjak, C. Vieh, R. Brun, Q. Xu, T. Yoshiie, Y. Dai, Positron annihilation spectroscopy of ferritic/martensitic steels F82H and T91 irradiated with protons and neutrons at PSI, J. Nucl. Mater. 450 (2014) 59–63, https://doi.org/10.1016/J.JNUCMAT.2013.09.009.
[49] W. Xu, L. Li, J.A. Valdez, M. Saber, Y. Zhu, C.C. Koch, R.O. Scattergood, Effect of nano-oxide particle size on radiation resistance of iron–chromium alloys, J. Nucl. Mater. 469 (2016) 72–81, https://doi.org/10.1016/J.JNUCMAT.2015.11.044.
[50] P.D. Edmondson, C.M. Parish, Y. Zhang, A. Hallén, M.K. Miller, Helium bubble distributions in a nanostructured ferritic alloy, J. Nucl. Mater. 434 (2013) 210–216, https://doi.org/10.1016/j.jnucmat.2012.11.049.
[51] Q. Li, C.M. Parish, K.A. Powers, M.K. Miller, Helium solubility and bubble formation in a nanostructured ferritic alloy, J. Nucl. Mater. 445 (2014) 165–174, https://doi.org/10.1016/j.jnucmat.2013.10.048.